RESEARCH PAPER

Gelatin Hydrogel/Magnetic Cobalt Nanoparticles Containing Pantoprazole for Adequate Drug Release

Reza Ahadzadeh and Azadeh Asefnejad *

Department of Biomedical Engineering, Science and Research Branch, Islamic Azad University, Tehran, Iran

ARTICLE INFO

Article History:
Received 06 June 2022
Accepted 17 September 2022
Published 01 October 2022

Keywords:
Cobalt-magnetic nanoparticles
Magnetic-Gelatin hydrogel
Pantoprazole

ABSTRACT

Gastric wound is the most common type of gastric ulcer with lots of complication when the protective mucosa inside the stomach becomes ineffective. The stomach produces strong acids to support digest food. As the mucosa loses its normal function, stomach acid may damage the stomach tissue and lead to stomach ulcers. Therefore, the need to develop new therapies with controlled function is well required in which one of the new solutions is to use magnetic hydrogels. In this regard, cobalt nanoparticles (Co-NP) were synthesized using molds made by anodizing technique and magnetic nanoparticles (MNPs) were loaded on gelatin hydrogel containing penaprazole. Scanning electron microscope (SEM), Fourier-transform infrared spectroscopy (FTIR), Energy-dispersive X-ray spectroscopy (EDS), and X-ray diffraction (XRD) was used to examine the morphology, functional group, and microstructure analysis of the samples. The EDS results indicate that the amount of Fe for both samples is in the range of 3-5 wt%. Also, investigation of magnetic properties of particles was performed using vibrating-sample magnetometer (VSM) test. The magnetization of sample A was 11.83 emu/g, which did not increase or decrease significantly compared to the value of sample B, 11.61 emu/g. Drug release occurred in about 70% within 48 hours and the effect of increasing gelatin on hydrogel on the rate of swelling was investigated. The obtained results indicated that with increasing the amount of gelatin, swelling significantly increased.

How to cite this article
Ahadzadeh R., Asefnejad A. Gelatin Hydrogel/Magnetic Cobalt Nanoparticles Containing Pantoprazole for Adequate Drug Release. J Nanostruct, 2022; 12(4):782-798. DOI: 10.22052/JNS.2022.04.002

INTRODUCTION

Gastric ulcers for a long time thought that factors such as eating spicy foods, stress, smoking and poor eating habits, and taking certain medications were the only causes of gastric ulcers until scientists discovered a bacterium in the gastric [1-4]. Researchers found that this bacterium was present in the stomach of many people called this bacterium “Helicobacter pylori. Gastric or peptic ulcer is the damage done to the lining of the stomach or small intestine [5-7]. This complication occurs when the protective mucosa inside the stomach becomes ineffective. The stomach produces strong acids to help digest food and to fight germs. As the mucosa loses its normal function, stomach acid can damage stomach tissue and lead to stomach ulcers [8-11]. Based on the available statistics, it is estimated that one in ten people may develop this disease during their lifetime. Treatment may vary depending on the

* *Corresponding Author Email: asefnejad@srbiau.ac.ir*

cause of the wound in the patient.

Most of the wounds can be treated with simple and basic treatments, only in rare cases surgery may be require in which prompt and timely treatment of gastric ulcer is very important [12-16]. Therefore, the use of drug-containing hydrogels can be effective. Gelatin is one of the biopolymers on the market that is used in medical applications due to its excellent compatibility, insecurity and very wide biodegradability [17-19]. Collagen-derived gelatin is used in clinics for wound dressing, pharmacy, and adhesives because of its compatibility, biodegradability, and hydrogel properties, as well as its formability and cost-effectiveness. However, unlike synthetic polymers, which are generally non-ionic, gelatin is a type of polyelectrolyte polymer that has a large number of ionizing groups.

In addition, strong hydrogen bonding leads to the formation of a 3D macromolecular network, which drastically reduces the mobility of gelatin chains [20-24]. Magnetic nanoparticles (MNPs) in nanoscale have different properties. Some elements or compounds, such as iron or iron oxides have magnetic properties that retain these properties in the nanoscale [25-39]. MNPs consist of a magnetic core and an ultra-magnetic outer shell in which the outer shell enhances the magnetic properties of the nanoparticles. The enhanced magnetic properties of MNPs allow for highly sensitive detection as well as reduced nanoparticle aggregation [40-45]. Magnetic nanoparticles are divided into three groups: ferromagnetic, paramagnetic and diamagnetic [46-51]. The property of diamagnetism is apparently found in all types of materials [52-54]. The present study aims to make magnetic nanoparticles and load drugs on gelatin hydrogel.

MATERIALS AND METHODS

Dissolve 10 g of $COSO_4.H_2O$ and 1 g of boric acid in 25 ml of deionized water. Place the cathode and anode of the electrolysis device in solution until MNPs are synthesized. The electrolysis process is performed at room temperature. After synthesis, the nanoparticles should be washed several times with distilled water. Pour the nanoparticles into a plate and place in the oven to dry completely. Then, mix the gelatin powder in 100 cc of deionized water. Three different amounts of gelatin are considered to find the optimal hydrogel. Finally, after the necessary experiments to investigate the magnetic properties, the synthesized nanoparticles are placed in a hydrogel by fusion method. According to the fusion method, first a magnetic fluid to avoid mass and oxidation by scattering of MNPs within the phase. Then, the mixture is combined with a hydrogel solution, and by crosslinking, the MNPs are encapsulated within the hydrogel structure.

Using UV, the crosslink process is performed for the hydrogel. Scanning electron microscope (SEM) is used for photographing surfaces and morphology of the hydrogel. X-ray diffraction (XRD) is a method for studying the microstructure of crystalline materials for shape and size of the building unit. The basis of the vibrating-sample magnetometer (VSM) is the Faraday induction law, which by vibrating the sample and applying a magnetic field to it, creates an inductive current in the coils embedded in the device. By transferring this inductive current to the computer connected to the device and displaying the waste loop, the magnetization of the sample can be measured.

Water absorption test is used and for this purpose, first the samples are weighed and after immersion in phosphate buffer saline (PBS), their weight eas measured again and the absorption rate may be obtained from Equation 1.

$$\text{Weight loss} = \text{W-W0/W0} * 100$$

In order to evaluate the stability and measure the rate of degradation in the external environment, the hydrolytic biodegradability test is used. At the end of every 24 hours, the dry weight of the compound was measured. Using the UV-Vis test, first the concentration of the drug is determined and then the concentration of the drug in the samples is examined. The test for measuring antibacterial properties is determined according to the relevant standard. Heterogeneous expression of genes in cancer cells that lead to diversity is called cellular parasitism. Cancer stem cells are cells that have the ability to self-regenerate and can differentiate into adult cancer cells. Cancer stem cells are similar to normal stem cells are very similar to normal stem cells in terms of self-renewal and metabolic properties. However, differences have been found between cancer and normal stem cells. Heat treatment methods can be divided into two main groups based on the technique used to generate heat: magnetic hyperthermia and heat optical

heat treatment methods [55-58]. Metal spinelite ferrite nanoparticles have the general relationship MFe_2O_4 that M can be metals such as Zn, Fe, Mg, Co, Ni, and Mn.

These applications of cobalt ferrite nanoparticles are due to their ability to distribute cationically among subnets in tetrahedral and octahedral sites [59-62]. Cobalt ferrite nanoparticles are widely regarded for their interesting properties such as magneto-crystalline anisotropy, high inductance, medium saturation magnetism, high chemical stability, abrasion resistance and electrical insulation. The magnetic properties of the material depend on the size, shape and purity of the nanoparticles. Among the various ferrites, ferrites on $ZnFe_2O_4$ and cobalt ferrites on $CoFe_2O_4$ have been studied more because they are ferrites usually with normal spinel and inverted spinel, respectively [50-62]. The Co-Fe cobalt-ferrite composite ferrites are very interesting for research due to their interesting and completely different properties of $ZnFe_2O_4$ ferrite and $CoFe_2O_4$ cobalt ferrite. Magnetic properties of cobalt spinelite ferrite structure can be changed by cationic substitution to a composite structure. Based on new studies, replacement of Zn^{2+} with CO_2 in cobalt nanoparticles of Co1-x Znx Fe_2O_4 has shown that properties such as chemical stability, high corrosion resistance, magneto-crystalline anisotropy, and magneto-optics have been improved. Thermotherapy is one of the treatment methods for cancer cells in which the temperature of cancer cells is raised to a temperature between 41°C and 45°C. In thermotherapy, a ferromagnetic or superparamagnetic compound is directed to the site of a cancer cell and then, by applying an external magnetic field, converts the strength of the external magnetic field into heat energy by applying several para or ferromagnetic particle mechanisms.

Zhang et al. [39] described $TiO_2/ZnCO_2O_4$ nanorods a strategy to achieve highly sensitive and selective detection of formaldehyde (HCHO) and triethylamine (TEA) using porous $ZnCO_2O_4$ nanorods used with TiO_2 as a marking agent Data. $TiO_2/ZnCo_2O_4$ nanorods were prepared by molding method, in which solid ZnC_2O_4/CoC_2O_4 nanorods were pre-synthesized using a deposition method at room temperature and then immersed as a model of porous TiO_2 nanorods. The $ZnCO_2O_4$ is used in $C_{10}H_{14}O_5Ti$ ethanol solution (before calcination) [35]. Accordingly, CoNWs-GO-PEGDOX demonstrates the satisfactory effect of killing cancer cells by chemotherapy *in vitro*. The present work provides a comprehensive overview of the potential of CoNWs-GO-PEG to serve as an antitumor agent in synergistic chemotherapeutic chemotherapy.

Heat treatment method that does not have the above defects has been used in the synthesis of various ferrites. In this research, researchers have synthesized cobalt ferrite nanoparticles on CoxZn1-xFe_2O_4 for (1, 0.8, 0.6, 0.4, 0.2 and x = 0) using heat treatment method and replacement effects of Co^{2+} with Zn^{2+} has been investigated for these nanoparticles. Initial anodizing was performed in 10% sulfuric acid solution and at 20 volts DC at 12°C for different times for sections A and B, 10 minutes and 30 minutes, respectively. To remove the surface oxide layer, a solution of 1% phosphoric acid was used at ambient temperature for 20 minutes. It should be noted that this solution may only remove the oxide layer created on the outer surface of the aluminum and may not damage the aluminum substrate.

Synthesis of nanoparticles

4 g of cobalt sulfate (4% wt) and add to 100 cc of deionized water was used in this study. After completion of the solution, the composition is removed from the electrolysis process. Electrolysis uses two electrodes made of aluminum and iron. After the electrolysis process, the obtained particles are poured into a falcon and used for better separation from the centrifuge for 10 minutes at a speed of 6000 rpm. After the particles inside the Falcon settle, the samples were washed several times with deionized water.

Table 1. Fabrication of magnetic hydrogels

sample code	(MNPs) Magnetic particles	Metronidazole: Penaprazole	Gelatin (G)	Sample
a	0.5 gr NP in 1 cc 5%G	1:1	5 gr G in 100 cc	5%G-NP
b	0.5 gr NP in 1 cc 10%G	1:1	10 gr G in 100 cc	10%G-NP
c	0.5 gr NP in 1 cc 15%G	1:1	15 gr G in 100 cc	15%G-NP
d	0.5 gr NP in 1 cc 20%G	1:1	20 gr G in 100 cc	20%G-NP

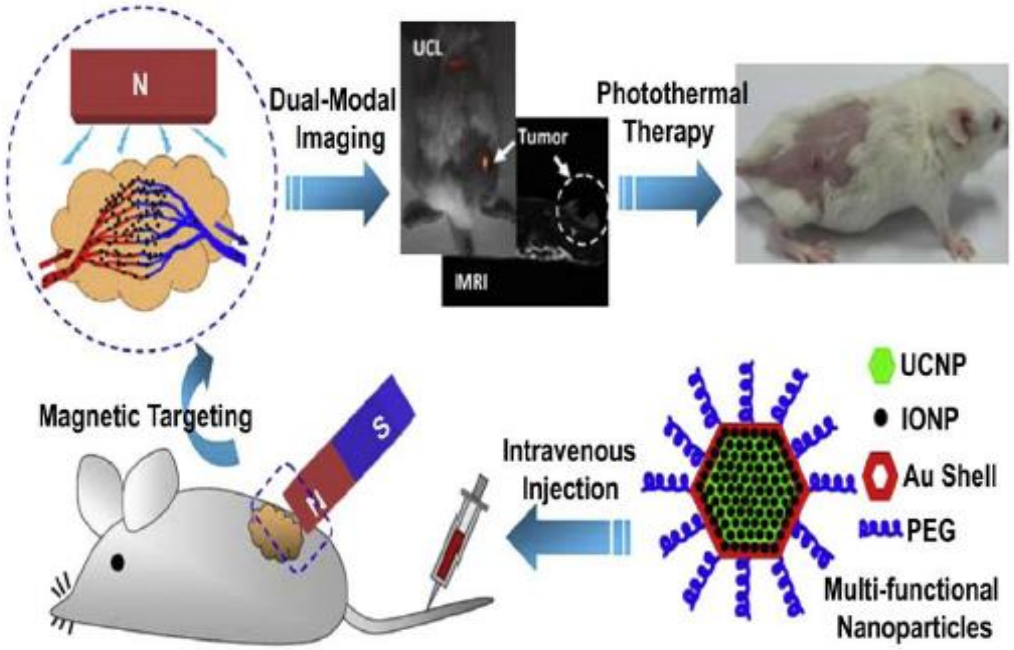

Fig. 1. Schematic application of gelatin hydrogel/cobalt magnetic nanoparticles containing penaprazole and magnetic conduction in the extracorporeal phase. The local magnetic field around the tumor tissue causes the accumulation of nanoparticles in the target tissue

Pour the particles into the plate and put the plate in the oven at 30°C for 24 hours to dry the water completely.

Gelatin hydrogels were prepared in different concentrations of 5, 10, 15 and 20 wt% using distilled water. Pantoprazole has been used for the combined treatment of gastrointestinal wound. In this article, metronidazole is used in addition to panaprazole. The nanoparticles made are mixed in the prepared solutions. In this study, mix 1 cc of gelatin hydrogel with 0.5 g of MNPs. The crosslinking process was performed on magnetic hydrogels using UV rays.

Table 1 shows the amount of material used for each magnetic hydrogel. Fig. 1 shows the schematic application of gelatin hydrogel/cobalt magnetic nanoparticles containing penaprazole and magnetic conduction in the extracorporeal phase. Fig. 2 shows the preparation technique for synthesize the gelatin hydrogel/cobalt magnetic nanoparticles after electrolysis.

Morphological study

Scanning electron microscope (SEM) analysis

Scanning electron microscopy (SEM: AIS2100) was used to evaluate the surface of MNPs and magnetic hydrogels. First, the samples were coated with gold and then imaging was performed and the nanoparticle size was measured using Image-J software. It may be possible to identify the constituent elements of the sample in semi-quantitative form. At least 5 mg of particle sample is required to analyze Energy dispersive spectroscopy (EDS) whicht may be calculated semi-quantitatively and the energy spectrum may be presented.

X-ray diffraction (XRD) analysis

To study the crystal structure and phase composition of the samples, X-ray diffraction (XRD) analysis was performed. X-ray wavelength is 1.54 A, copper anode and nickel filter. The stop time in each step was one second, the step size was 0.02 degrees and the sweeping range (2θ) was selected between 10 and 80° and the patterns were identified using references.

Vibrating-sample magnetometer (VSM)

Magnetometers measure the magnetization of a sample of material with different dimensions

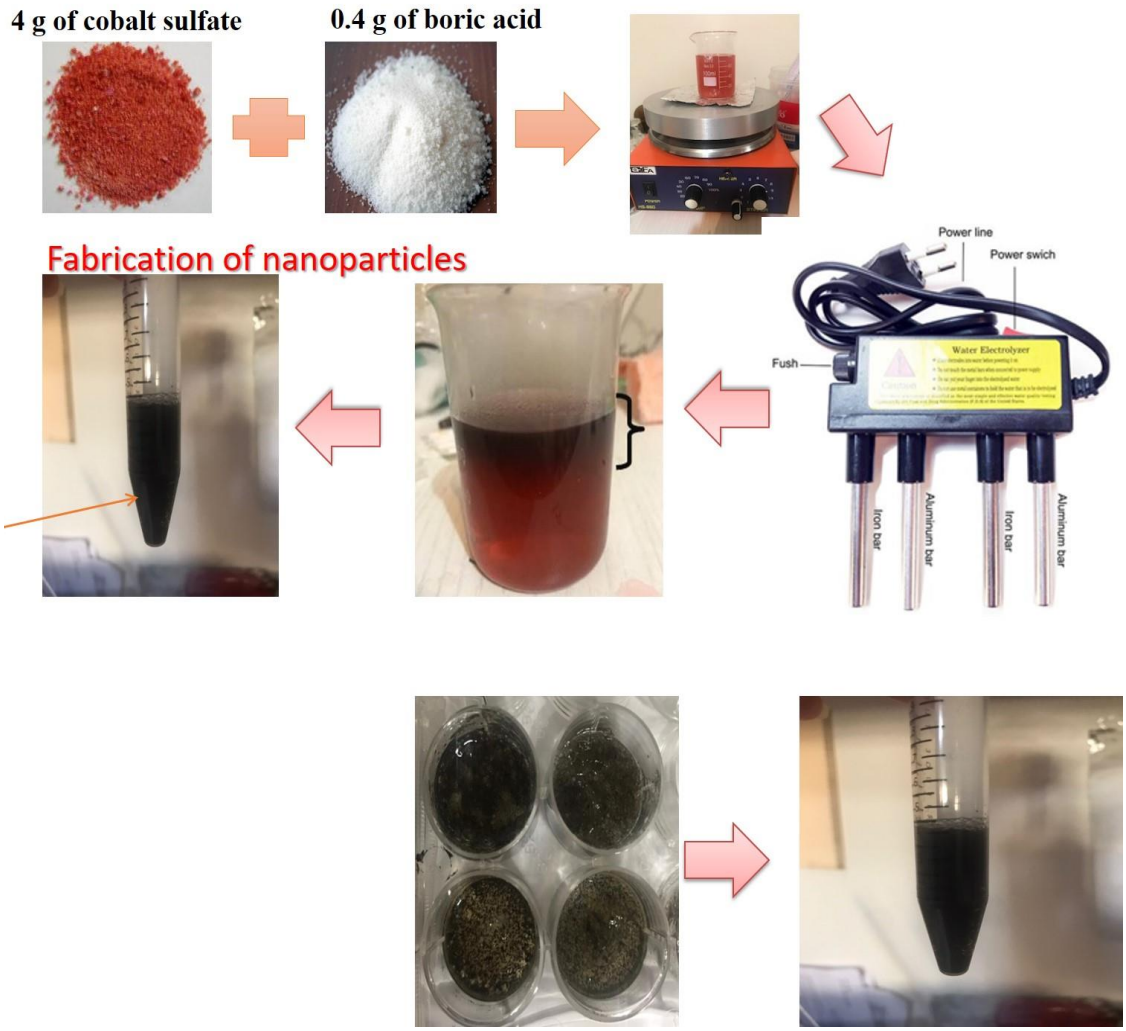

Fig. 2. Schematic of preparation and characterization of gelatin hydrogel/cobalt magnetic nanoparticles after electrolysis

in different ways and under different conditions of temperature, magnetic field and sample orientation. The basis of the VSM magnetometer is the Faraday induction law, which, by vibrating the sample and applying a magnetic field to it, creates an inductive current in the coils embedded in the device that is proportional to the sample's magnetism. This device is able to measure the magnetic properties of materials in powder and liquid state and thin layer up to 1.5 Tesla field.

Inflation evaluation

To evaluate the amount of water absorption on coated and uncoated scaffolds. The scaffolds sample placed in a PBS. Swelling was performed for all hydrogels containing MNPs. In order to evaluate the rate of degradation in the external environment. For this purpose, first the dry weighed scaffold was placed in PBS for 7 days. Every 24 hours a sample was taken out of solution and dried on filter paper and the weight of the sample was measured. The percentage of biodegradability of scaffold is obtained from the following equation.

$$\text{Biodegradability} = [(\text{W-W0})/\text{W0}] \times 100$$

Where W0 is the dry weight and W is the weight of the immersed scaffold. Swelling was performed for all hydrogels containing MNPs.

Antibacterial behaviour

One of the methods for measuring the antibacterial properties of a substance is the method of determining the diameter of the growth inhibition zone. The test specimens are then transferred to the culture medium. After storing the plates in the incubator for 24 hours at a temperature of 37°C, the plates are examined under light and the non-growth area is measured. Antibiogram classifies bacteria into susceptible, semi-susceptible or resistant groups based on qualitative results. Therefore, this method is a basic tool for determining the type of resistance phenotype among the tested bacteria. Gram-positive Staphylococcus bacteria are completely dispersed by Hooke into petri dishes containing solid LB medium based on McFarland concentration. Using disk fusion method, necessary studies have been performed for S. aureus (gram positive) and E. coli (gram negative) bacteria. These discs were completely sterilized by UV rays for 12 hours. Bacteria were completely dispersed by Hooke based on McFarland concentration into petri dishes containing solid LB medium. Finally, the plates were transferred to an incubator at 37°C and stored for 24 hours. The halo created around

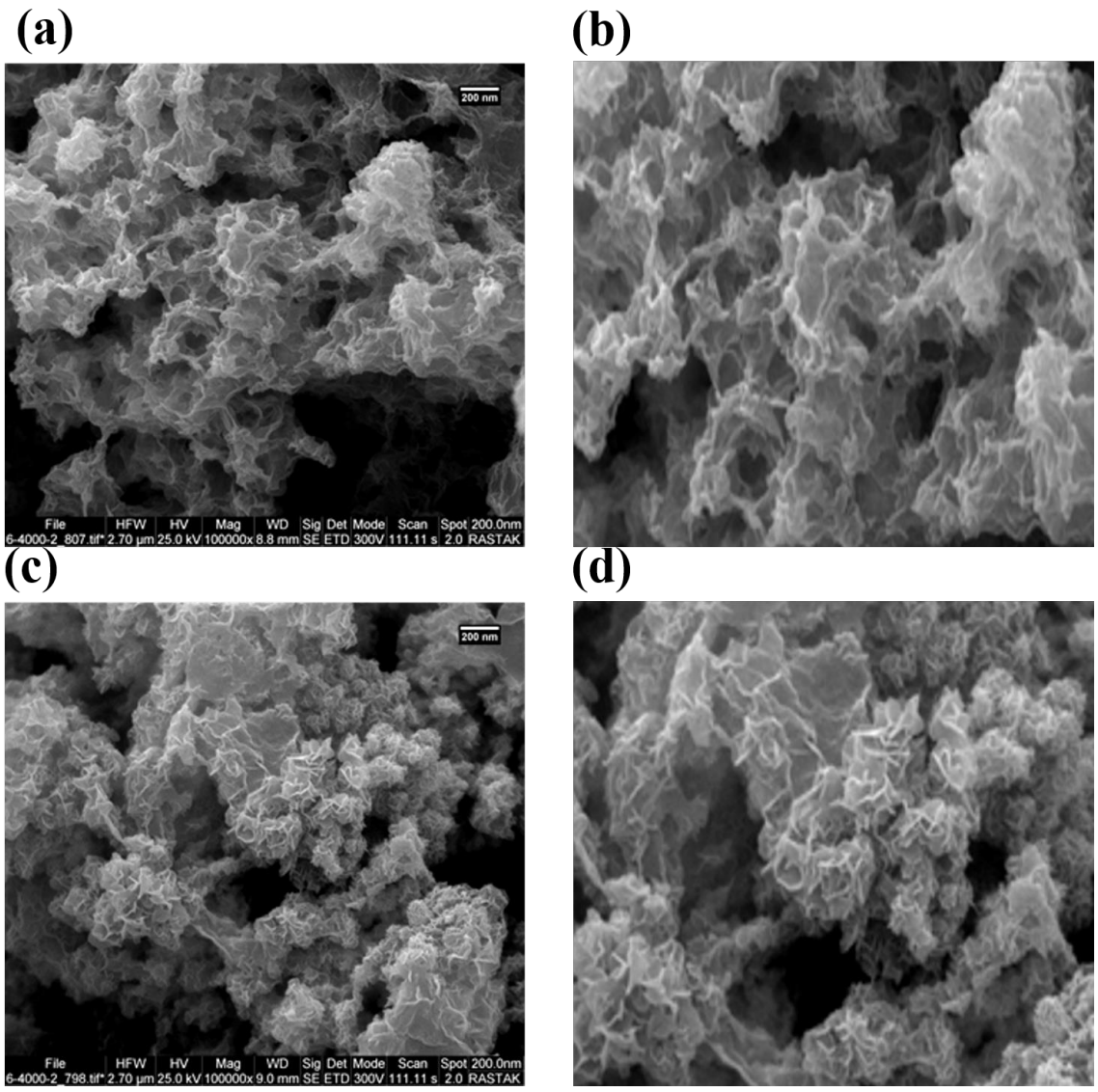

Fig. 3. SEM microscope image of particles obtained with: a-b) fragment A, c-d) fragment B

the specimens reflects the antibacterial properties of the scaffold.

Drug release analysis

The initial concentration of Pantoprazole and metronidazole is 2 ppm. To draw a standard curve, the drugs were diluted with PBS and prepared in 4 concentrations. Then, the absorbance of the samples was measured by UV spectrophotometer. To prepare the dialysis bag for the release test, the dialysis bag was placed in a solution containing 2 wt% baking soda and 0.05 wt% EDTA for 30 minutes. It was washed twice with distilled water and again placed in boiling distilled water. Insert 4 mg of magnetic hydrogel into the dialysis bag and close the top of the bag with another clip. 30 ml of PBS solution was poured into the human dialysis bag containing the samples. Sampling was performed at different intervals and the same amount of new solution was used instead. The samples were then placed in a UV spectrophotometer and a graph was plotted by calculating the release percentage of the drug released from the hydrogel.

Tensile strength analysis

The data obtained in this test are used to determine the mechanical properties of the material. Tensile strength or ultimate tensile strength (UTS) is the maximum tensile stress that the specimen can withstand and the ratio of the maximum force (load) to the initial cross-section of the specimen is defined. The slope of the linear part of the stress-strain curve is the elastic modulus. The samples were glued to the paper frame according to ISO-6824 standard with dimensions of 10.60 mm and were subjected to tensile strength test and compared. The paper frame was placed between the two jaws of the traction machine at a distance of 3 cm with an applied force of 10 N, a traction speed of 10 mm/min, a humidity of 30%.

RESULTS AND DISSCUSION

Fig. 3 (a-b) shows the morphological

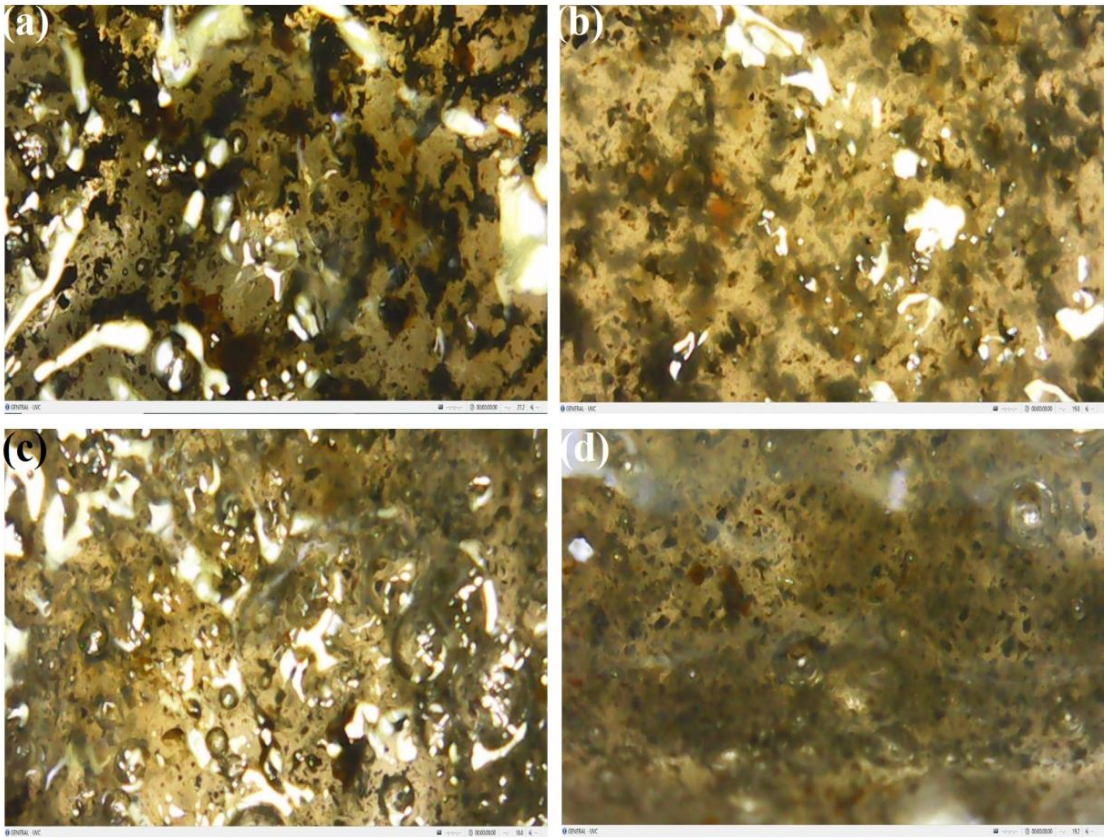

Fig. 4. Optical microscope image: a) 5% G-NP, b) 10% G-NP, C) 15% G-NP, d) 20% G-NP

examination using a SEM image for nanoparticles synthesized in this study. Fig. 3(a) shows the particles obtained by block A and Fig. 3(b) is for the particles obtained by block B. As can be seen in the obtained images, the difference in the anodizing parameters has caused the particles to have slight changes in terms of morphology.

Fig. 4 shows a magnetic hydrogel after the blending process. Fig. 4 shows the light microscope image of a magnetic hydrogel. Fig. 4 indicates the MNPs are evenly distributed throughout the gelatin hydrogel. Fig. 5 (a) shows the XRD analysis of samples A and B. The XRD pattern is very wide for samples A and B obtained by anodizing aluminum parts. The taller and narrower the spikes, the more crystalline the material, and the wider and shorter the material, the closer it is to the amorphous form. The anodizing process has resulted in rod nanoparticles being structurally irregular. The obtained peaks represent cobalt sulfate, calcium phosphate hydrate ($CaPO_3(OH)_2H_2O$) and boric acid (H_3BO_3). Sobhani et al. [47] study showed that $CoSO_4H_2O$ has a monoclinic phase (space group C2 = c) by fixed network n = 0.695, b = 0.757 nm and c = 0.762 with card number 2104-70 = JCPDS It is [45]. Card numbers 0293-011-00 and 1455-072-01 are related to CaPs hydrate and cobalt sulfate, respectively. The peaks related to calcium phosphate hydrate for sample A are equal to 2θ = 29.2° and 2θ = 44.92° and for sample B are equal to 28.24° = 2θ and θ2 = 44.56 °. The cobalt sulfate peaks for samples A and B are around θ = 44.62 and θ2 = 45.3, respectively. Peaks of 10/48 (sample A) and 56/48 (sample B) are related to boric acid, which is consistent with the studies of Liu et al. [46].

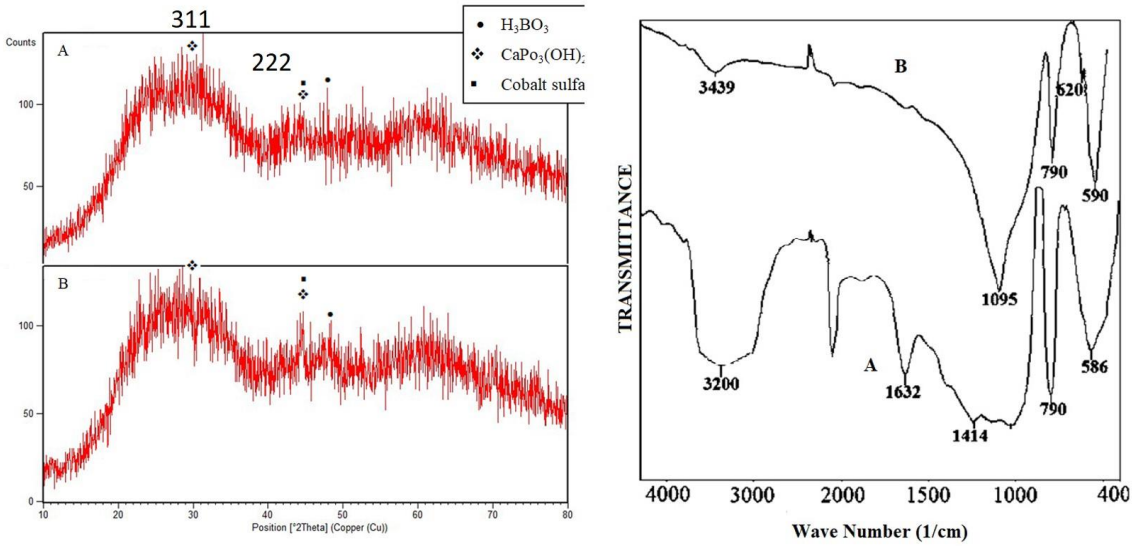

Fig. 5. XRD and FTIR pattern of samples of peaks of 10/48 (sample A) and 56/48 (sample B) are related to boric acid

Table 2. X-ray diffraction analysis of samples A and B.

	$CaPO_3(OH)_2H_2O$		Cobalt sulfat		H_3BO_3	
	A	B	A	B	A	B
Peak(2θ°) 00-011-0293	29.02° 44.92°	28.4° 44.56°	---	---	---	---
Peak (2θ°) 01-072-1455	---	---	44.62°	45.3°	---	---
Peak (2θ°)		---		---	48.10°	48.56°

Fig. 5 (b) shows the FTIR spectrum of the as-prepared sample. In this spectrum, absorption band from 3500 cm^{-1} to 2350 cm^{-1} is the features of stretching vibration of OH which indicates the availability of H_2O in the hydrogel. In addition, strong absorption bands at 790, 1080, 1414 cm^{-1} and 1632 cm^{-1} which may be assigned vibration mode of ring structure of SiO_2 tetrahedra.

Fig. 6 shows the presence of elements in samples A and B using EDS analysis. Accordingly, the EDS graph shows the rates of available chemical elements such as cobalt (Co), oxygen (O), carbon (C), iron (Fe), silicon (Si) and sulfur (S). Figs. 6 shows the presence of elements in particles A and B, which for cobalt, oxygen, carbon, iron, silicon and sulfur in particles A are 67.15, 14.92, 4.48, and 77, respectively. Also, the mentioned values for B particles are equal to 79.67, 9.02, 0.78, 3.52, 1.37 and 5.64 percent, respectively. The highest percentage of weight of cobalt is related to sample B.

Fig. 6 (b-bc) shows the results of the Map micrograph. The distribution of iron and cobalt elements in samples A and B is evenly distributed

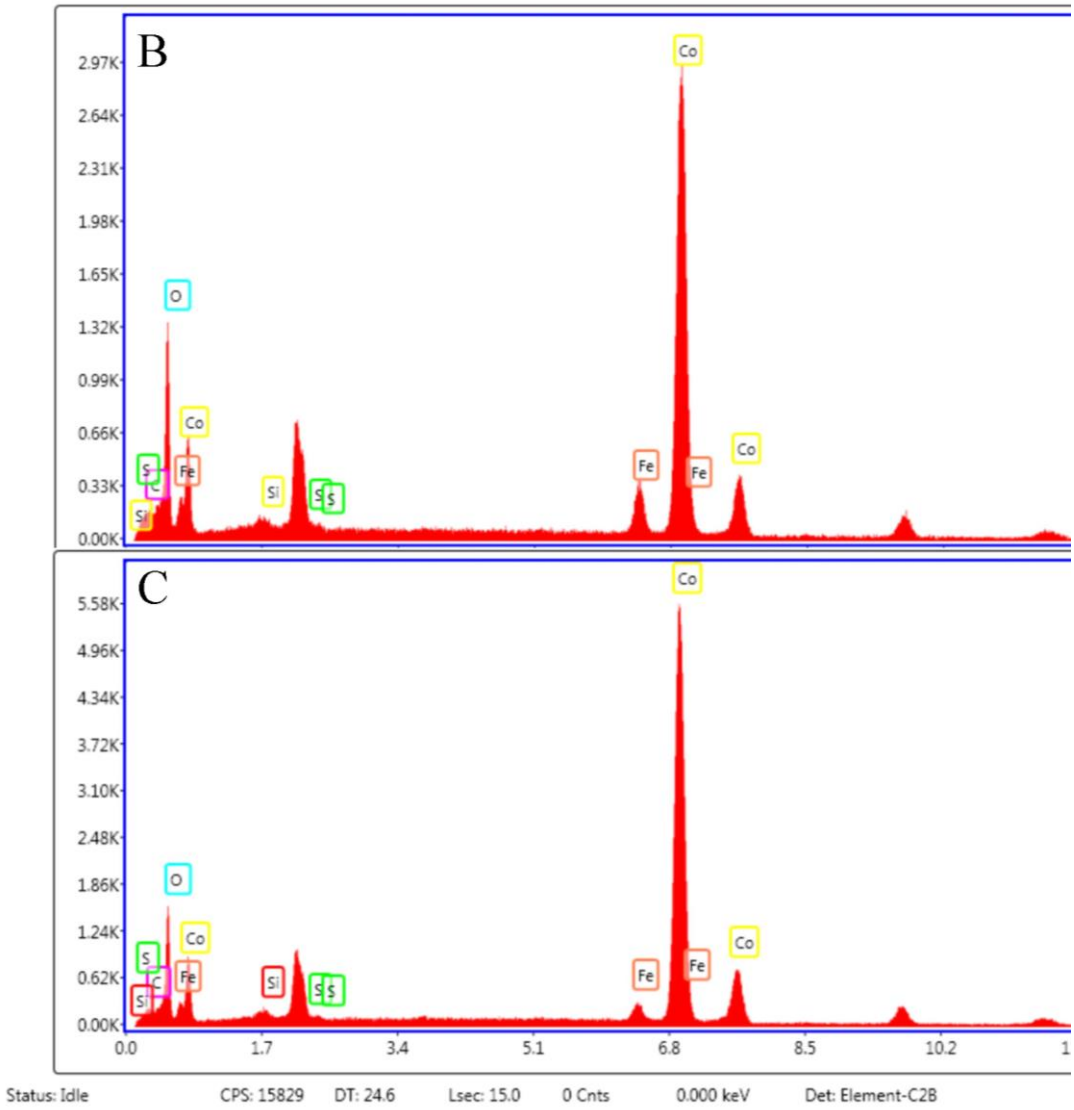

Fig. 6. EDS micrograph of elements present in particles A and B defined for cobalt, oxygen, carbon, iron, silicon and sulfur in the particles

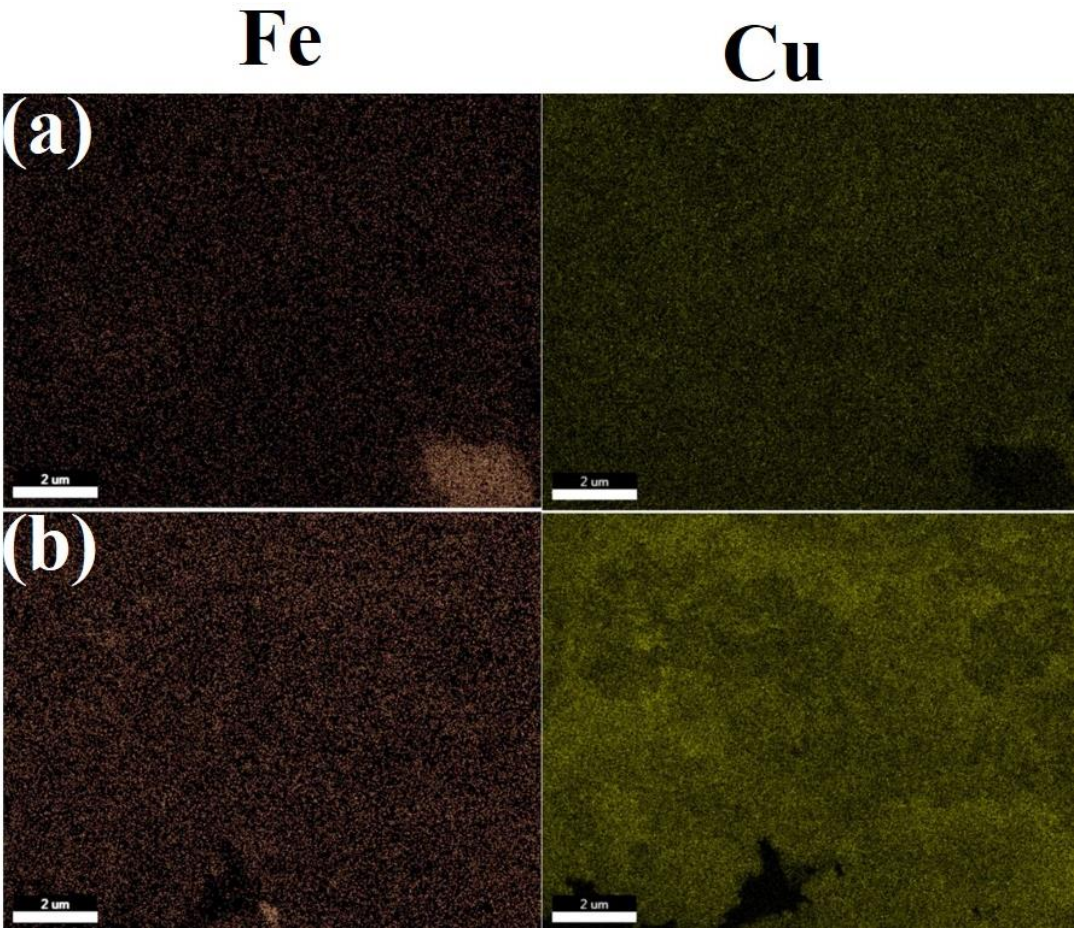

Fig. 7. Results of the Map micrograph of distributed iron and cobalt elements in samples A and B uniformly in different areas of the sample

and uniform is established in different areas of the sample. Metals with semi-solid orbitals such as pure iron and cobalt have magnetic properties in which this group of metal solids is called ferromagnetic material [48]. The amount of drug loading in the hydrogel and the amount of drug release from them were measured by UV spectroscopy. The magnetic behavior of samples A and B can be measured using a VSM device by plotting the residual curve. The diagram of the magnetic effect of the synthesized particles, at ambient temperature and in the fields of 10,000 to 10,000 overs, is shown in Fig. 7. The results at this stage indicate the initial explosive release in the range of 30-50% of the loaded drugs. For the ferromagnetic properties of particles, the dispersion of iron and cobalt elements is of particular importance. Map micrograph examination shows the proper dispersion of both elements in both materials as shown in Fig. 7.

Fig. 8 shows the percentage of drug release from the hydrogel in the PBS. The area under the peak was calculated for all concentrations at 203 nm and finally the standard drug concentration curve was plotted in terms of UV uptake. The line diagram equation of standard drugs was obtained $0.0001 + x = 0.001$ with $R^2 = 1$ as shown in Fig. 8. As can be seen, the magnetization of sample A, 11.83 emu/g was obtained, which did not decrease or increase significantly compared to sample B, 11.61 emu/g.

Based on VSM analysis, the superparamagnetic structure in sample B is confirmed. The absence of a residual ring in the VSM diagram indicates superparamagnetic behavior and the magnetic property of magnetite is very sensitive to the

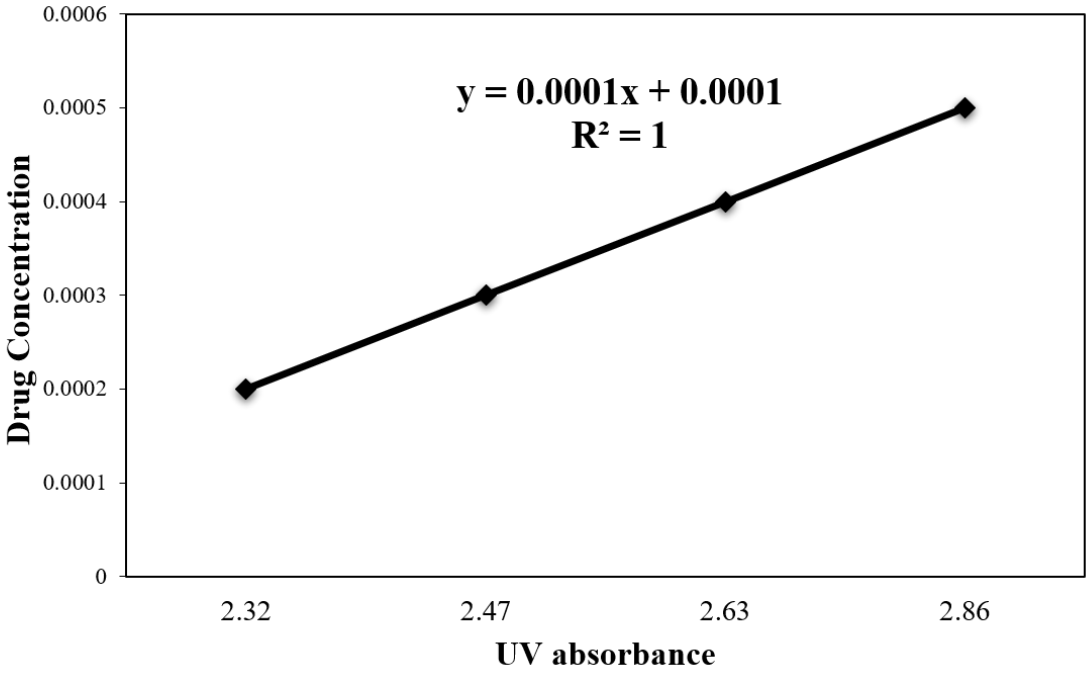

Fig. 8. Standard curve of drugs

structure of the sample and the superparamagnetic property occurs when the particles are small enough that thermal fluctuations can cause magnetic changes as shown in Fig. 9.

The absence of a residual loop in the VSM profile is an important criterion required for the superparamagnetic behavior of nanoparticles [50-55]. Drug release occurred in five stages with different slopes as shown in Fig. 10. In stage (d) up to 24 hours about 70% of the release has occurred. In the last step, the slope of the graph is almost fixed and the drug concentration inside and outside the films is the same. The results of the drug release test indicate release in the form of control infiltration. The study of swelling and water absorption properties in the hydrogel network is essential in various applications. In this study, the effect of increasing gelatin on hydrogel on swelling was investigated. Fig. 11 demonstrate the amount of gelatin increases and then the swelling rate increased too. The sample with 20% gelatin showed the highest swelling up to 233.33%. By far the lowest amount of gelatin is the percentage of swelling up to 44.74%. As the amount of gelatin increases in the first hour, more water is absorbed into the hydrogels.

Scaffolds with 5% and 10% were destroyed after 5 hours. Also, 15% and 20%G scaffolds were destroyed after 6 and 7 hours. This release rate is due to the degradation of surface abrasion of the hydrogel along with the release of drugs adhering to the sample surface as shown in Fig. 12. The slope of the release chart is reduced at this stage. However, at this stage, an increase in the release percentage of up to 60% is observed, which is due to the occurrence of the penetration phenomenon inside the hydrogel and the continued degradation of the polymer. In the third stage (c), which occurs in the range of 15 hours to 20 hours after the start of the test, the slope of the graph is almost constant.

Destruction for sample with 20% reinforcement in scaffold after 6 hours is 83.33%. The demolition time of the specimens is consistent with studies by Wiwatwongwana et al. [51]. They stated that compositing gelatin with another polymer such as carboxy methyl cellulose increases the degradation time in the hydrogel. Because the hydrogel is structurally stronger, but the pure gelatin hydrogel is degraded within 9 hours [51].

Fig. 13 (a-b) investigation of antibacterial properties of 20% G-NP sample containing

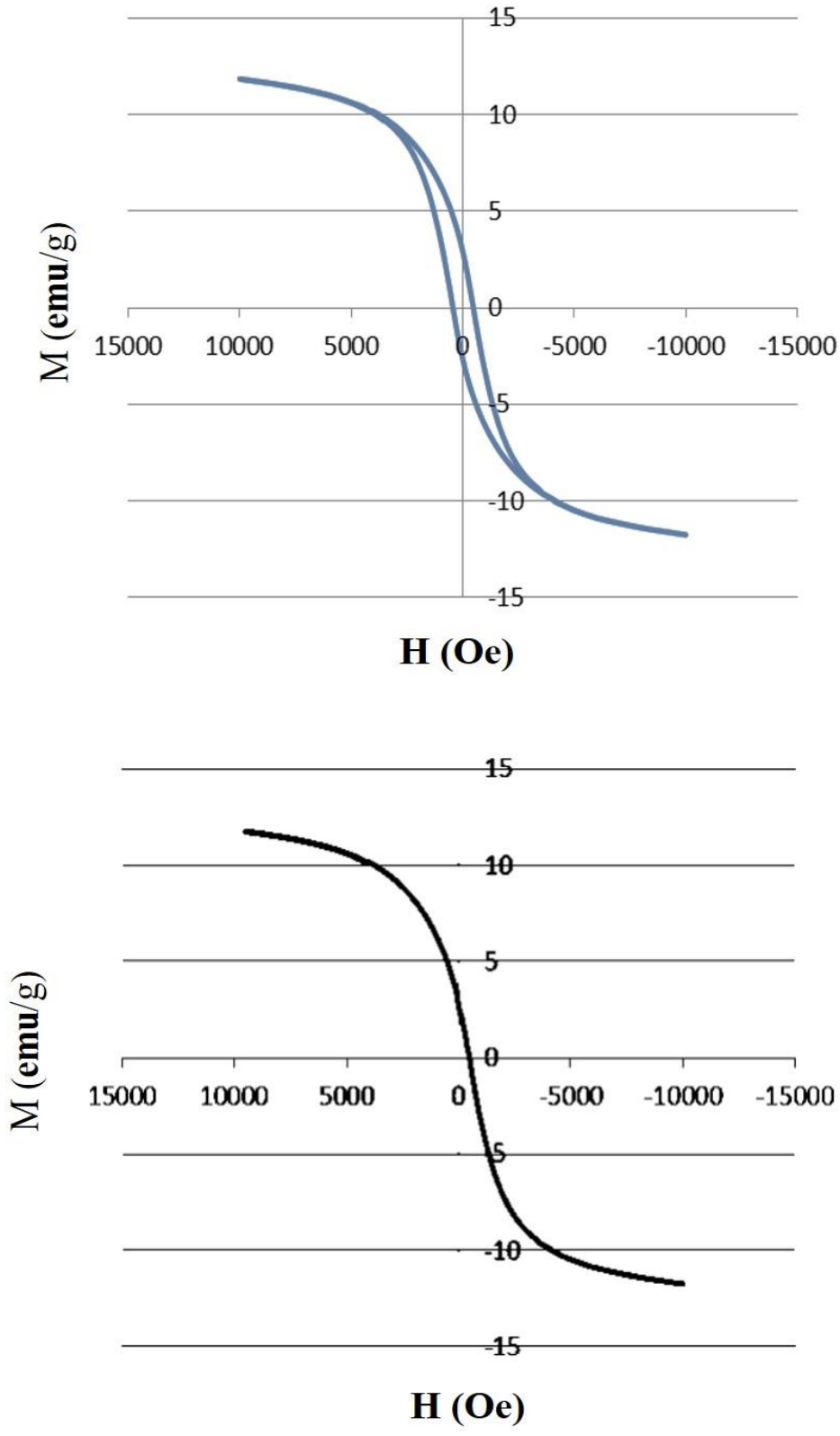

Fig. 9. Magnetic behavior of samples A and B measured using a VSM device by plotting the residual curve

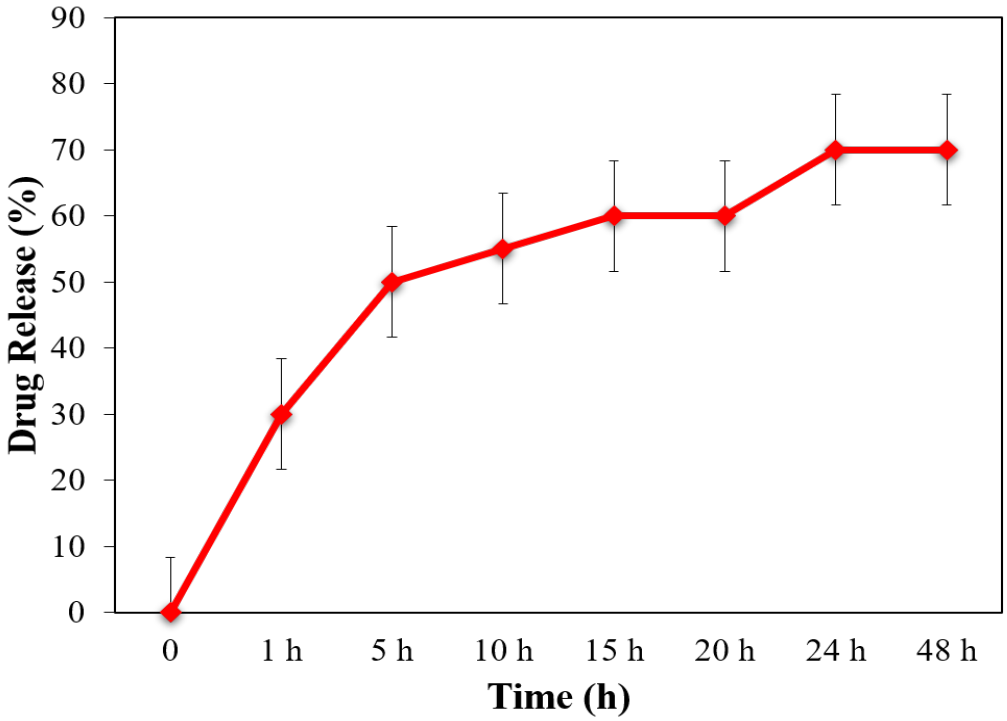

Fig. 10. Drug release percentageous after two days of incubation

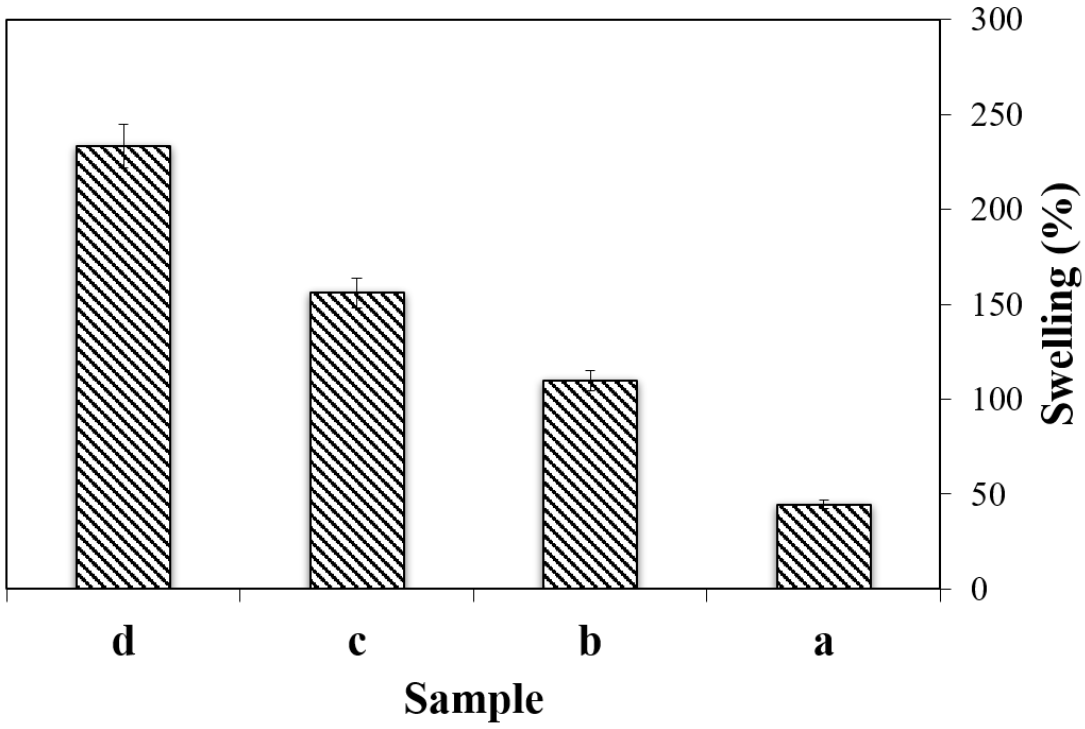

Fig. 11. Swelling rateof a) 5% G - NP, b) 10% -NP, C) 15% -NP, and d) 20% -NP

metronidazole and penaprazole.

The mechanical properties of biological materials are critical among the parameters because they have a significant impact on cell behavior. The vascular system of the skin undergoes intermittent cyclic deformation, showing elastic modulus in the range of 25.2-130 MPa depending on the physiological anatomy, location and function of blood vessels. Therefore, the mechanical properties of scaffolds with different concentrations of gelatin have been investigated using tensile test and the results are

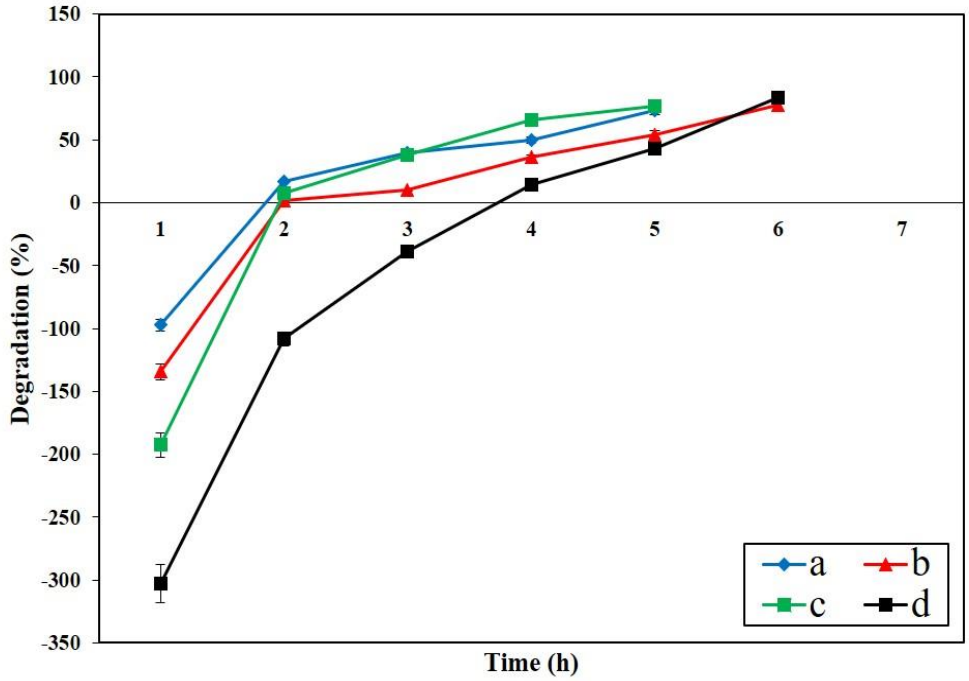

Fig. 12. Biodegradability chart: a) 5% G-NP, b) 10% G-NP, C) 15% G-NP, d) 20% G-NP

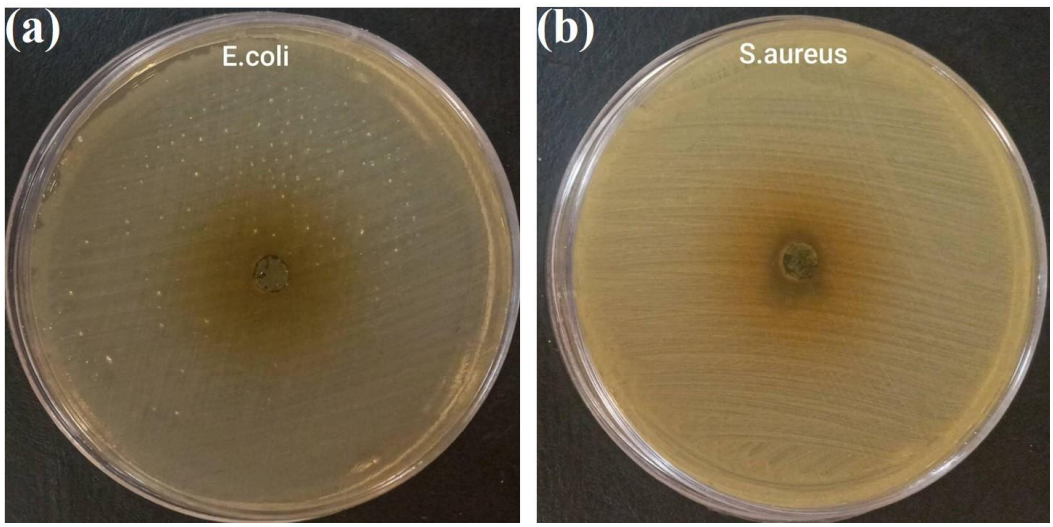

Fig. 13. Antibacterials tests for S. aureus (gram positive) and E. coli (gram negative) bacteria sterilized by UV for 12 hours.

Table 3. Investigation of mechanical properties such as elastic modulus and tensile test

Sample	Force (N)	Tensile (mm)	Stress (MPa)	Elongation (%)
20%G -NP	0/481	13/4958	4/81	44/986
15%G -NP	0/594	9/5695	5/94	31/8982

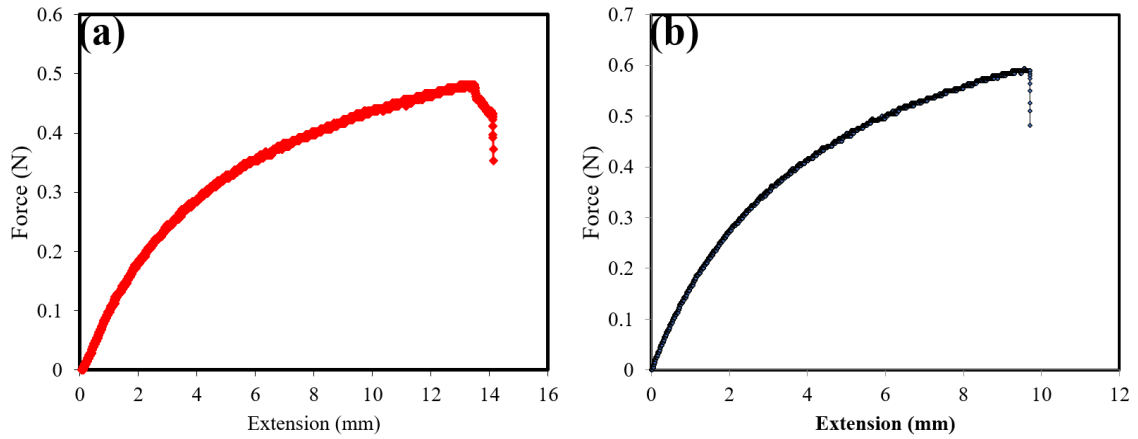

Fig. 14. Force-extension diagram derived from tensile strength of samples a) 20% G-NP, b) 15% G-NP

according to Table 3.

Fig. 14 shows a diagram of the mechanical properties of 15% -NP and 20% -NP samples. As can be seen from the diagram, the amount of scaffold tension has also increased with increasing gelatin amount. As shown in Table 3, the percentage of elongation for the 20% G-NP sample is 44.98%. With decreasing gelatin amount, the percentage of elongation has decreased and reached to 31.89%.

CONCLUSION

Treatment of gastric wound is one of the most important challenges facing medical knowledge and drug delivery. Treatment of gastric wound with magnetic hydrogel can be directed to the target tissue by magnetic particles and with continuous release which leads to faster healing process. In this study, magnetic nanoparticles have been prepared using electrolysis process. The solution is prepared by cobalt (II) sulfate and boric acid. Using the anodizing process, porosities were created on the surface of the components. Modifications have been made to the anodizing process for both templates to identify the best parameter. It can be stated that placing the mold in a solution of sulfuric acid for 30 minutes is optimal. Gelatin hydrogels are prepared and the desired drugs are added to the solution. Using the blending technique, the optimal magnetic nanoparticles were loaded into the hydrogel. Morphological studies have shown that the anodizing process affects the morphology of the deposited particles. Microstructural studies using XRD pattern show peaks related to calcium phosphate, hydrate, cobalt sulfate, and boric acid. The EDS micrograph showed the highest amount of trace elements for cobalt and iron. The scattering of two elements with magnetic properties such as iron and cobalt is well shown in the map. VSM test studies have shown that nanoparticles obtained from anodized mold have superparamagnetic properties for a longer period of time. Drug release occurred in about 70% within 48 hours. The swelling test for the sample containing 20% gelatin showed the highest absorption rate up to 233%. Most detoration occurred after 6 hours for sample containing 20% gelatin in hydrogel. The pores created around the magnetic hydrogel was an evidence of the antibacterial property of the sample. Mechanical properties using tensile test have shown that with increasing gelatin amount,

the elongation has increased from 31% to 44%.

ACKNOWLEDGEMENTS

The authors would like to extend their gratitude for the support provided by department of Biomedical Engineering, Science and Research Branch, Islamic Azad University, Tehran, Iran.

CONFLICT OF INTEREST

The authors declare that there is no conflict of interests regarding the publication of this manuscript.

REFERENCE

1. Djagny KB, Wang Z, Xu S. Gelatin: A Valuable Protein for Food and Pharmaceutical Industries: Review. Critical Reviews in Food Science and Nutrition. 2001;41(6):481-492.
2. Exploratory Study of 3D Printed Biodegradable Cervical Interbody Fusion Cage. Case Medical Research. 2019.
3. Salmani MM, Hashemian M, Yekta HJ, Nejad MG, Saber-Samandari S, Khandan A. Synergic Effects of Magnetic Nanoparticles on Hyperthermia-Based Therapy and Controlled Drug Delivery for Bone Substitute Application. Journal of Superconductivity and Novel Magnetism. 2020;33(9):2809-2820.
4. Tavan H, Sayehmiri K, Abangah G, Kalvandi G, Aazami S. Prevalence of peptic ulcer in Iran: Systematic review and meta-analysis methods. J Res Med Sci. 2018;23(1):8.
5. Abdellahi M, Najfinezhad A, Saber-Samanadari S, Khandan A, Ghayour H. Zn and Zr co-doped M-type strontium hexaferrite: Synthesis, characterization and hyperthermia application. ChJPh. 2018;56(1):331-339.
6. Sufi SA, Hoda M, Pajaniradje S, Mukherjee V, Coumar SM, Rajagopalan R. Enhanced drug retention, sustained release, and anti-cancer potential of curcumin and indole-curcumin analog-loaded polysorbate 80-stabilizied PLGA nanoparticles in colon cancer cell line SW480. Int J Pharm. 2020;588:119738.
7. Dariva CG, Figueiredo JPH, Ferreira C, Laranjo M, Botelho MF, Fonseca AC, et al. Development of red-light cleavable PEG-PLA nanoparticles as delivery systems for cancer therapy. Colloids Surf B Biointerfaces. 2020;196:111354.
8. Abastabar M, Akbari A, Akhtari J, Hedayati MT, Shokohi T, Mehrad-Majd H, et al. In vitro antitumor activity of patulin on cervical and colorectal cancer cell lines. Current Medical Mycology. 2017;3(1):25-29.
9. Zhang Y, Wu M, Han X, Wang P, Qin L. High-Throughput, Label-Free Isolation of Cancer Stem Cells on the Basis of Cell Adhesion Capacity. Angew Chem Int Ed. 2015;54(37):10838-10842.
10. Hergueta-Redondo M, Peinado H. The influence of secreted factors and extracellular vesicles in ovarian cancer metastasis. Eur J Cancer Suppl. 2020;15:38-48.
11. Valastyan S, Weinberg Robert A. Tumor Metastasis: Molecular Insights and Evolving Paradigms. Cell. 2011;147(2):275-292.
12. Kumar CSSR, Mohammad F. Magnetic nanomaterials for hyperthermia-based therapy and controlled drug delivery. Adv Drug Del Rev. 2011;63(9):789-808.
13. Issels RD. Hyperthermia adds to chemotherapy. Eur J Cancer. 2008;44(17):2546-2554.
14. Gao L, Fei J, Zhao J, Li H, Cui Y, Li J. Hypocrellin-Loaded Gold Nanocages with High Two-Photon Efficiency for Photothermal/Photodynamic Cancer Therapy in Vitro. ACS Nano. 2012;6(9):8030-8040.
15. Zhang W, Yamamoto H. Vanadium-Catalyzed Asymmetric Epoxidation of Homoallylic Alcohols [Am. Chem. Soc.2007, 129, 286−287]. Journal of the American Chemical Society. 2007;129(16):5298-5298.
16. Hu K-W, Liu T-M, Chung K-Y, Huang K-S, Hsieh C-T, Sun C-K, et al. Efficient Near-IR Hyperthermia and Intense Nonlinear Optical Imaging Contrast on the Gold Nanorod-in-Shell Nanostructures. Journal of the American Chemical Society. 2009;131(40):14186-14187.
17. Yang K, Wan J, Zhang S, Tian B, Zhang Y, Liu Z. The influence of surface chemistry and size of nanoscale graphene oxide on photothermal therapy of cancer using ultra-low laser power. Biomaterials. 2012;33(7):2206-2214.
18. Jasemi A, Kamyab Moghadas B, Khandan A, Saber-Samandari S. A porous calcium-zirconia scaffolds composed of magnetic nanoparticles for bone cancer treatment: Fabrication, characterization and FEM analysis. Ceram Int. 2022;48(1):1314-1325.
19. Cheng L, Yang K, Li Y, Zeng X, Shao M, Lee S-T, et al. Multifunctional nanoparticles for upconversion luminescence/MR multimodal imaging and magnetically targeted photothermal therapy. Biomaterials. 2012;33(7):2215-2222.
20. Wust P, Hildebrandt B, Sreenivasa G, Rau B, Gellermann J, Riess H, et al. Hyperthermia in combined treatment of cancer. The Lancet Oncology. 2002;3(8):487-497.
21. Ghayour H, Abdellahi M, Ozada N, Jabbrzare S, Khandan A. Hyperthermia application of zinc doped nickel ferrite nanoparticles. Journal of Physics and Chemistry of Solids. 2017;111:464-472.
22. Hydrogels: Types, Structure, Properties, and Applications. Frontiers in Biomaterials Volume 4: Bentham Science Publishers Ltd. p. 143-169.
23. Shaheen T, Edirisinghe T, Gabriel M, Bourdoumis A, Buchholz N, Knight M. In vitro encrustation of a semi-permanent polymer-covered nitinol ureter stent: an artificial urine model. Urolithiasis. 2014;42(3):203-207.
24. Farazin A, Sahmani S, Soleimani M, Kolooshani A, Saber-Samandari S, Khandan A. Effect of hexagonal structure nanoparticles on the morphological performance of the ceramic scaffold using analytical oscillation response. Ceram Int. 2021;47(13):18339-18350.
25. Liu Y, Li T, Han Y, Li F, Liu Y. Recent development of electrospun wound dressing. Current Opinion in Biomedical Engineering. 2021;17:100247.
26. Nuge T, Tshai KY, Lim SS, Nordin N, Hoque ME. Characterization and optimization of the mechanical properties of electrospun gelatin nanofibrous scaffolds. World Journal of Engineering. 2020;17(1):12-20.
27. Heydari-Meybodi M, Saber-Samandari S, Sadighi M. An experimental study on low-velocity impact response of nanocomposite beams reinforced with nanoclay. Composites Science and Technology. 2016;133:70-78.
28. Gu S-Y, Wang Z-M, Ren J, Zhang C-Y. Electrospinning of gelatin and gelatin/poly(l-lactide) blend and its characteristics for wound dressing. Materials Science and Engineering: C. 2009;29(6):1822-1828.
29. Samadian H, Salehi M, Farzamfar S, Vaez A, Ehterami A, Sahrapeyma H, et al. In vitro and in vivo evaluation of electrospun cellulose acetate/gelatin/hydroxyapatite nanocomposite mats for wound dressing applications. Artificial Cells, Nanomedicine, and Biotechnology. 2018;46(sup1):964-974.
30. İnal M, Mülazımoğlu G. Production and characterization of bactericidal wound dressing material based on gelatin nanofiber.

Int J Biol Macromol. 2019;137:392-404.
31. Farazin A, Torkpour Z, Dehghani S, Mohammadi R, Fahmy MD, Saber-Samandari S, et al. A Review on Polymeric Wound Dress for the Treatment of Burns and Diabetic Wounds. International Journal of Basic Science in Medicine. 2021;6(2):44-50.
32. Nosrati H, Pourmotabed S, Sharifi E. A Review on Some Natural Biopolymers and Their Applications in Angiogenesis and Tissue Engineering. Journal of Applied Biotechnology Reports. 2018;5(3):81-91.
33. Abdellahi M, Jabbarzare S, Ghayour H, Khandan A. Thermal and X-ray analyses of aluminum–titanium nanocomposite powder. Journal of Thermal Analysis and Calorimetry. 2017;131(2):853-863.
34. Khandan A, Karamian E, Faghih M, Bataille A. Formation of AlN Nano Particles Precipitated in St-14 Low Carbon Steel by Micro and Nanoscopic Observations. Journal of Iron and Steel Research International. 2014;21(9):886-890.
35. Sivudu KS, Rhee KY. Preparation and characterization of pH-responsive hydrogel magnetite nanocomposite. Colloids Surf Physicochem Eng Aspects. 2009;349(1-3):29-34.
36. Soleimani M, Asgharzadeh Salmasi A, Asghari S, Joneidi Yekta H, Kamyab Moghadas B, Shahriari S, et al. Optimization and fabrication of alginate scaffold for alveolar bone regeneration with sufficient drug release. International Nano Letters. 2021;11(3):295-305.
37. Saeedi M, Abdellahi M, Rahimi A, Khandan A. Preparation and characterization of nanocrystalline barium ferrite ceramic. Functional Materials Letters. 2016;09(05):1650068.
38. Zhang B, Li Y, Luo N, Xu X, Sun G, Wang Y, et al. $TiO_2/ZnCo_2O_4$ porous nanorods: Synthesis and temperature-dependent dual selectivity for sensing HCHO and TEA. Sensors Actuators B: Chem. 2020;321:128461.
39. Zhu H, Deng J, Yang Y, Li Y, Shi J, Zhao J, et al. Cobalt nanowire-based multifunctional platform for targeted chemo-photothermal synergistic cancer therapy. Colloids Surf B Biointerfaces. 2019;180:401-410.
40. Kenawy E, Omer AM, Tamer TM, Elmeligy MA, Eldin MSM. Fabrication of biodegradable gelatin/chitosan/cinnamaldehyde crosslinked membranes for antibacterial wound dressing applications. Int J Biol Macromol. 2019;139:440-448.
41. Jabbarzare S, Abdellahi M, Ghayour H, Arpanahi A, Khandan A. A study on the synthesis and magnetic properties of the cerium ferrite ceramic. Journal of Alloys and Compounds. 2017;694:800-807.
42. Mahnken AH, Buecker A, Wildberger JE, Ruebben A, Stanzel S, Vogt F, et al. Coronary Artery Stents in Multislice Computed Tomography. Invest Radiol. 2004;39(1):27-33.
43. Caffarena VdR, Capitaneo JL, Simão RA, Guimarães AP. Preparation of electrodeposited cobalt nanowires. Materials Research. 2006;9(2):205-208.
44. Sobhani A, Salavati-Niasari M. Facile Hydrothermal Synthesis of $CoSO_4ċH_2O$ Nanoparticles and Barite Microcubes from Novel Precursors. High Temp Mater Processes (London). 2012;31(6):711-715.
45. Liu J, Liang D, Xiao J, Chen B, Zhang Y, Zhou J, et al. Composition and characteristics of primary combustion products of boron-based propellants. Combustion, Explosion, and Shock Waves. 2017;53(1):55-64.
46. Seok JH, Choi HS, Jung S-L, Ahn K-J, Kim MJ, Shin YS, et al. Artificial Luminal Narrowing on Contrast-Enhanced Magnetic Resonance Angiograms on an Occasion of Stent-Assisted Coiling of Intracranial Aneurysm:In Vitroi Comparison Using Two Different Stents with Variable Imaging Parameters. Korean J Radiol. 2012;13(5):550.
47. Karimi Z, Mohammadifar Y, Shokrollahi H, Asl SK, Yousefi G, Karimi L. Magnetic and structural properties of nano sized Dy-doped cobalt ferrite synthesized by co-precipitation. Journal of Magnetism and Magnetic Materials. 2014;361:150-156.
48. Cole AJ, Yang VC, David AE. Cancer theranostics: the rise of targeted magnetic nanoparticles. Trends Biotechnol. 2011;29(7):323-332.
49. Fan L, Luo C, Li X, Lu F, Qiu H, Sun M. Fabrication of novel magnetic chitosan grafted with graphene oxide to enhance adsorption properties for methyl blue. J Hazard Mater. 2012;215-216:272-279.
50. Wiwatwongwana F, Chaijit S. Mechanical Properties Analysis of Gelatin/Carboxymethylcellulose Scaffolds. International Journal of Materials, Mechanics and Manufacturing. 2019;7(3):138-143.
51. Ghiyasiyan-Arani M, Salavati-Niasari M. Comparative study on electrochemical hydrogen storage of nanocomposites based on S or N doped graphene quantum dots and nanostructured titanium niobate. Journal of Alloys and Compounds. 2022;899:163379.
52. Monsef R, Soofivand F, Abbas Alshamsi H, Al-Nayili A, Ghiyasiyan-Arani M, Salavati-Niasari M. Sonochemical synthesis and characterization of $PrVO_4$/CdO nanocomposite and their application as photocatalysts for removal of organic dyes in water. J Mol Liq. 2021;336:116339.
53. Ghiyasiyan-Arani M, Salavati-Niasari M, Zonouz AF. Effect of Operational Synthesis Parameters on the Morphology and the Electrochemical Properties of 3D Hierarchical AlV_3O_9 Architectures for Li-Ion Batteries. Journal of The Electrochemical Society. 2020;167(2):020544.
54. Ghiyasiyan-Arani M, Salavati-Niasari M. Strategic design and electrochemical behaviors of Li-ion battery cathode nanocomposite materials based on AlV3O9 with carbon nanostructures. Composites Part B: Engineering. 2020;183:107734.
55. Ghiyasiyan-Arani M, Salavati-Niasari M. Synergic and coupling effect between SnO_2 nanoparticles and hierarchical AlV_3O_9 microspheres toward emerging electrode materials for lithium-ion battery devices. Inorganic Chemistry Frontiers. 2021;8(11):2735-2748.
56. Doozandeh Z, Saber-Samandari S, Khandan A. Preparation of Novel Arabic Gum-C6H9NO Biopolymer as a Bedsore for Wound Care Application. Acta Med Iran. 2020.
57. Prasad A, Kandasubramanian B. Fused deposition processing polycaprolactone of composites for biomedical applications. Polymer-Plastics Technology and Materials. 2019;58(13):1365-1398.
58. Karimi M, Asefnejad A, Aflaki D, Surendar A, Baharifar H, Saber-Samandari S, et al. Fabrication of shapeless scaffolds reinforced with baghdadite-magnetite nanoparticles using a 3D printer and freeze-drying technique. Journal of Materials Research and Technology. 2021;14:3070-3079.
59. Lenhart M, Völk M, Manke C, Nitz WR, Strotzer M, Feuerbach S, et al. Stent Appearance at Contrast-enhanced MR Angiography: In Vitro Examination with 14 Stents. Radiology. 2000;217(1):173-178.
60. Razavi M, Khandan A. Safety, regulatory issues, long-term biotoxicity, and the processing environment. Nanobiomaterials Science, Development and Evaluation: Elsevier; 2017. p. 261-279.
61. Mirzadeh S, Asefnejad A, Khonakdar HA, Jafari SH. Improved surface properties in spray-coated PU/TiO2/graphene hybrid nanocomposites through nonsolvent-induced phase separation. Surface and Coatings Technology. 2021;405:126507.
62. Janfada A, Asefnejad A, Khorasani MT, Joupari MD. Reinforcement of electrospun polycaprolacton scaffold using KIT-6 to improve mechanical and biological performance. Polym Test. 2020;84:106391.